

Article

Open Access



NiS nanoparticle-MoS₂ nanosheet core-shell spheres: PVP-assisted synthesis and efficient electrocatalyst for hydrogen evolution reaction

Gabriel Engonga Obiang Nsang¹, Badshah Ullah¹, Sun Hua¹, Sayyar Ali Shah^{1,4,*} , Nabi Ullah², Noor Ullah¹, Flora Ngozi Dike¹, Waleed Yaseen³, Aihua Yuan^{1,*}, Naseem Khan¹, Habib Ullah^{4,*}

¹School of Environmental & Chemical Engineering, Jiangsu University of Science and Technology, Zhenjiang 212003, Jiangsu, China.

²Department of Inorganic and Analytical Chemistry, Faculty of Chemistry, University of Lodz, Lodz 91-403, Poland.

³School of Chemistry and Chemical Engineering, Jiangsu University, Zhenjiang 212013, Jiangsu, China.

⁴Department of Engineering, Faculty of Environment, Science and Economy, University of Exeter, Exeter EX4 4QF, UK.

***Correspondence to:** Dr. Sayyar Ali Shah, School of Environmental & Chemical Engineering, Jiangsu University of Science and Technology, Zhenjiang 212003, Jiangsu, China; Department of Engineering, Faculty of Environment, Science and Economy, University of Exeter, Exeter EX4 4QF, UK. E-mail: sayyarali83@just.edu.cn; Dr. Aihua Yuan, School of Environmental & Chemical Engineering, Jiangsu University of Science and Technology, Zhenjiang 212003, Jiangsu, China. E-mail: aihua.yuan@just.edu.cn; Dr. Habib Ullah, Department of Engineering, Faculty of Environment, Science and Economy, University of Exeter, Exeter EX4 4QF, UK. E-mail: Hu203@exeter.ac.uk

How to cite this article: Obiang Nsang, G. E.; Ullah, B.; Hua, S.; Shah, S. A.; Ullah, N.; Ullah, N.; Dike, F. N.; Yaseen, W.; Yuan, A.; Khan, N.; Ullah, H. NiS nanoparticle-MoS₂ nanosheet core-shell spheres: PVP-assisted synthesis and efficient electrocatalyst for hydrogen evolution reaction. *Energy Mater.* **2025**, *5*, 500047. <https://dx.doi.org/10.20517/energymater.2024.134>

Received: 23 Aug 2024 **First Decision:** 16 Oct 2024 **Revised:** 17 Dec 2024 **Accepted:** 30 Dec 2024 **Published:** 20 Feb 2025

Academic Editors: Ho Won Jang, Xili Tong **Copy Editor:** Fangling Lan **Production Editor:** Fangling Lan

Abstract

The synthesis of an effective, robust, and cost-efficient electrocatalyst for H₂ through water electrolysis is crucial for developing clean and sustainable energy technology. Herein, we report polyvinylpyrrolidone-assisted synthesis of NiS nanoparticle-MoS₂ nanosheets core-shell (NiS@MoS₂) spheres as an efficient electrocatalyst for the hydrogen evolution reaction (HER) using the hydrothermal method. The polyvinylpyrrolidone controls the size and morphology of the NiS@MoS₂ sphere, and it converts into N-doped carbon (NC) as a conductive material during the calcination process to form NiS@MoS₂/NC spheres. The change in MoS₂ concentration (NiS@MoS₂/NC_x) of different catalysts significantly influences the material, size, and electrocatalytic performance. NiS@MoS₂/NC₅₀ exhibits excellent HER performance, showing a small Tafel slope of 56.7 mV dec⁻¹ and good stability with an overpotential of 189 mV at a current density of 10 mA cm⁻². HER performance is believed to be enhanced by the synergistic interaction between NiS nanoparticles and MoS₂ nanosheets at the heterointerface. Furthermore, NC



© The Author(s) 2025. **Open Access** This article is licensed under a Creative Commons Attribution 4.0 International License (<https://creativecommons.org/licenses/by/4.0/>), which permits unrestricted use, sharing, adaptation, distribution and reproduction in any medium or format, for any purpose, even commercially, as long as you give appropriate credit to the original author(s) and the source, provide a link to the Creative Commons license, and indicate if changes were made.



enhances the conductivity of the NiS@MoS₂/NC_x composites to enhance HER performance. Density Functional Theory simulations indicate that the best catalytic site of NiS@MoS₂ is Mo, where optimal electron transfer occurs between MoS₂ nanosheets and NiS nanoparticles. This electron transfer promotes H⁺ adsorption, reducing Gibbs free energy ($\Delta G_{H^*} \approx 0.04$ eV) and requiring a work function of 4.81 eV, thereby boosting HER performance. This work will open a low-cost approach for synthesis of non-precious core-shell electrocatalysts with high activity and stability for HER.

Keywords: Electrocatalyst, hydrogen evolution reaction, hydrothermal method, NiS nanoparticle-MoS₂ nanosheets core-shell, synergistic effect

INTRODUCTION

The rapid depletion of fossil energy resources and the decline in environmental quality have become increasingly critical challenges for both technology and modern society. Developing sustainable green energy sources is essential to address both energy crises and environmental issues. Hydrogen stands out as an ideal secondary energy source and a promising alternative to fossil fuels, offering high efficiency and non-pollution benefits^[1,2]. Electrochemical water splitting is a good strategy to produce sustainable green hydrogen^[3,4] due to its zero-carbon emission. This process involves two half-cell reactions: the hydrogen evolution reaction (HER) at the cathode and the oxygen evolution reaction (OER) at the anode, and thermodynamically, 1.23 V is required for the overall reaction to occur^[5-7]. However, these reactions suffer from significantly large overpotential because of slow reaction kinetics during the water-splitting process^[8,9]. A highly effective electrocatalyst is required to accelerate the OER and HER process to produce hydrogen from water splitting at low overpotential^[10]. Platinum (Pt)-based materials are known for their high activity and effectiveness as electrocatalysts for HER^[11]. Nevertheless, the limited availability and high cost of Pt-based materials have restricted their widespread use. Consequently, there is a growing focus on exploring sustainable and cost-effective electrocatalytic materials to replace precious metal-based catalysts^[12,13].

In recent decades, nanostructured materials with appropriate adsorption-desorption-free energies (ΔG_H) have been designed to enhance water-splitting electrocatalysis. Molybdenum disulfide (MoS₂) materials have attracted huge attention for hydrogen generation due to their unique electronic structure and close to zero free energy (ΔG_H)^[14,15]. Furthermore, the exposed edges of MoS₂ monolayers contain catalytic active sites, and their electronic properties facilitate the adsorption and dissociation of water molecules to release H⁺ and generate hydrogen gas^[16]. Researchers have explored various strategies to optimize the catalytic activity of MoS₂ nanomaterials for HER, including interface^[17], disorder engineering^[18], basal plane activation^[19], hetero-atoms doping^[20,21], expanded interlayer spacing^[22], hybridizing with other materials^[23], and designing different morphology^[24]. However, the catalytic HER performance of MoS₂ is suffering from a larger overpotential and still cannot be compared to that of Pt-based materials^[25-27]. Recent advances in core-shell heterojunction structures have demonstrated significant potential to enhance efficiency in the HER^[28,29]. These structures combine a core that provides structural integrity with a shell that improves catalytic activity and stability, optimizing charge separation, reducing recombination, and increasing active surface area. Notable examples include catalysts such as CoP@CoOOH^[30] and MoS₂@Ni₃S₂^[31], which show remarkable electrochemical performance improvements due to their structural design and composition. However, challenges remain, such as stability under operational conditions, optimization of core-shell interfaces, and scalability of synthesis methods. Additionally, while noble metals are highly efficient, their high cost limits practical applications, prompting the search for more affordable alternatives such as transition metal phosphides and sulfides. Efforts are also focused on techniques such as doping to fine-tune electronic properties and further enhance catalytic activity^[32,33].

MoS₂-based composites have become promising candidates for exceptional HER performance. These composite materials take advantage of the catalytic capabilities of MoS₂ nanomaterials and the added unique properties of the partnering materials, resulting in improved HER performance. Recently, MoS₂/NiS heterojunction composite has been reported and demonstrated excellent HER performance and durability^[34–36]. Chen *et al.* reported NiS and MoS₂ nanostructure composite and optimized heterostructure material for high-performance HER activity in both acidic and alkaline environments^[37]. Zhao *et al.* designed a heterostructure MoS₂/NiS nanoflowers through precise interface modification to improve its performance in HER, which is vital for sustainable hydrogen production^[38]. However, the low conductivity of the MoS₂/NiS composites remains an issue during the HER process. A conductive material generally combined with MoS₂/NiS materials can further improve its HER performance^[39]. Guan *et al.* presented a scalable method for growing NiS-MoS₂ hetero-nanosheet arrays on a carbon cloth and displayed outstanding HER performance due to a synergistic effect between NiS and MoS₂^[40]. Tao *et al.* synthesized NiS/MoS₂ nanowire and nanoflake electrocatalysts on carbon matrix by hydrothermal-electrodeposition method and exhibited remarkable catalytic activity for HER in alkaline media^[41]. Recently, Liu *et al.* designed MoS₂/NiS heterostructures by a one-step synthesis method that exhibits superior HER performance, aiming to enhance their catalytic activity for HER^[42]. The conductive materials in the NiS-MoS₂ core-shell heterojunction, along with achieving a controllable morphology and stable structure, remain challenging. Our group has reported on the *in-situ* selective loading of NiS₂ nanoparticles onto MoS₂ nanosheet spheres, which are anchored on reduced graphene oxide to enhance HER performance^[43]. Considering pioneering works, the novel NiS-MoS₂ composites were designed for enhanced HER using: (i) polyvinylpyrrolidone (PVP) as a substrate in synthesis process and providing conductive N-doped carbon (NC) in the final composites; and (ii) Sulfides were chosen because these compounds usually display higher conductivity compared to oxides. Mo and Ni precursors in appropriate amounts formed the heterojunction composite and undoubtedly induced a synergistic effect for the catalytic process. In the composite, conductive materials were well distributed in the NiS-MoS₂ core-shell heterojunction with controllable morphology and stable structure for enhancement.

Here, we report the PVP-assisted synthesis of NiS nanoparticle-MoS₂ nanosheets core-shell spheres (herein named NiS@MoS₂/NC_x) by hydrothermal methods and display an excellent HER performance. The PVP controlled the size of the NiS@MoS₂/NC sphere and provided conductive NC support to the NiS@MoS₂ composites. Changing the concentration of the Mo precursor significantly influences the electrocatalytic performance of NiS@MoS₂/NC_x composites. The optimal NiS@MoS₂/NC₅₀ sample demonstrates excellent HER performance with overpotentials of 189 mV at a current density of 10 mA cm⁻² and excellent stability in a 1.0 M KOH solution. Density functional theory (DFT) simulations indicate that NiS@MoS₂ exhibits outstanding catalytic activity due to efficient charge transfer between NiS nanoparticles and MoS₂ nanosheets. This results in optimal H⁺ adsorption on the Mo site, reducing Gibbs free energy ($\Delta G_{H^*} \approx 0.04$ eV) and enhancing HER performance. The experimental data and computational results of the NiS@MoS₂/NC heterojunction composite may offer future perspectives for the synthesis of 3D metal sulfide and MoS₂ core-shell electrocatalysts for improved HER performance.

EXPERIMENTAL

Materials

Nickel sulfate hexahydrate [NiSO₄·6H₂O (50 mg)] (99.9%) and PVP (C₆H₉NO) were purchased from Shanghai McLean Biochemical Technology, Ammonium molybdate (para) tetrahydrate (NH₄)₆Mo₇O₂₄·4H₂O and thiourea (CH₄N₂S) were purchased from Shanghai Wokai Biotechnology. Commercial 20 wt% Pt/C was purchased from McLean Biotechnology. All the reagents were used as received without further purification.

Synthesis of NiS@MoS₂/NC_x composite

Firstly, PVP (200 mg) is dispersed in distilled water by sonication for 20 min. Then, ammonium molybdate tetrahydrate (NH₄)₆Mo₇O₂₄·4H₂O (50 mg) is added and dissolved into the PVP solution. This is followed by the dissolution of Nickel sulfate hexahydrate (NiSO₄·6H₂O) and thiourea CH₄N₂S in the reaction mixture. The mixture was placed in a Teflon-lined stainless-steel autoclave with a capacity of 30 mL and subjected to heating at 180 °C for 12 h. Once cooled, the product was retrieved through centrifugation and subsequently washed four times each with water and ethanol. The product was then dried at 50 °C for 15 h in a vacuum oven. Finally, it underwent calcination at 600 °C for 2 h. Various NiS@MoS₂/NC_x samples were synthesized using different quantities of (NH₄)₆Mo₇O₂₄·4H₂O, as detailed in [Supplementary Table 1](#), where "x" represents the amount of (NH₄)₆Mo₇O₂₄·4H₂O used.

Synthesis of NiS@MoS₂ composite

The same procedure without PVP was adopted for the synthesis of the NiS@MoS₂ composite. The precursors (NH₄)₆Mo₇O₂₄·4H₂O (50 mg), NiSO₄·6H₂O (50 mg), and CH₄N₂S (1,000 mg) were reacted together in the absence of PVP [[Supplementary Table 1](#)].

Synthesis of MoS₂/NC and NiS/NC composite

The MoS₂/NC and NiS/NC composites were prepared using the same procedure. For the MoS₂/NC sample, [(NH₄)₆Mo₇O₂₄·4H₂O (50 mg)] and CH₄N₂S reacted in the presence of a PVP solution. In contrast, for the NiS/NC synthesis, NiSO₄·6H₂O and CH₄N₂S were used as precursors in the reaction mixture with PVP [[Supplementary Table 1](#)].

Microstructure characterization

An X-ray powder diffractometer (XRD, Shimadzu XRD -6000) was used to characterize the crystal phases of as-prepared samples. A scanning electron microscope (SEM, FEI 250) and a transmission electron microscope [high-resolution transmission electron microscopy (HRTEM), JEOL JEM-2100F] were used to analyze the morphologies and microstructures of the materials. Energy-dispersive X-ray spectroscopy coupled with transmission electron microscopy (TEM) was used to scan the elemental mapping images. A Raman scattering spectrum was acquired at ambient temperature utilizing a Renishaw inVia Confocal Raman Microscope. A fully integrated X-ray photoelectron spectroscopy (Thermo Scientific Nexsa) was used to produce X-ray photoelectron spectra (XPS). The Thermogravimetric Analysis [Pyris Diamond TG-DTA (TGA)] was used to measure weight change in the temperature range of 25 to 800 °C at the heating rate of 10 °C min⁻¹ in air.

Electrochemical measurements

The electrochemical tests of the samples were conducted in a three-electrode system connected to the electrochemical workstation. A glassy carbon (GC), graphite rod, and Hg/HgO served as the working, auxiliary, and reference electrodes, respectively. To create a uniform ink from the synthesized catalysts and commercial 20 wt% Pt/C, 4 mg of the catalyst and 30 µL of a 5 wt% Nafion solution were sonicated in a 1:1 mixture of ethanol and deionized water (970 µL total). Subsequently, 5 µL of the resulting ink was applied to a GC electrode and left to dry in ambient conditions. Before linear sweep voltammetry (LSV), a cyclic voltammogram (CV) was performed for 20 cycles between 0 and -1.6 V vs. Hg/HgO. LSV curves were recorded in 1.0 M KOH solution at a scan rate of 5 mV s⁻¹. The double-layer capacitance (Cdl) was assessed within a potential range of 0-0.1 V vs. Hg/HgO across varying scan rates (10-100 mV s⁻¹) to evaluate the electrochemically active surface area (EASA) of the catalysts. The electrochemical active surface area (ECSA) normalized LSV curves of a catalyst were calculated as

$$\text{ECSA} = C_{dl}/C_s,$$

where C_s is the specific capacitance of the sample in the 1M KOH electrolyte condition, with a value of 0.040 mF cm^{-2} for tests conducted in the same electrolyte. Concurrently, electrochemical impedance spectroscopy (EIS) was conducted under identical conditions, covering frequencies from 100 kHz to 0.01 Hz. The stability of the catalyst was examined over 1,000 to 5,000 cyclic voltammetry (CV) cycles at a scan rate of 100 mV s^{-1} , within a potential window of 0 to $-1.6 \text{ V vs. Hg/HgO}$. LSV measurements were repeated after every 1,000 cycles to verify sample stability. Additionally, a chronoamperometry (i-t) curve was recorded over a 50-h period to assess long-term durability.

Computational approach

We employed spin-polarized DFT calculations to study the catalytic systems using Quantum ATK and visualized the structures using VESTA and VNL (version 2019.12). The aim was to simulate the core-shell architecture of NiS nanoparticles within MoS_2 nanosheets. Our first step was to construct the bulk model for MoS_2 , followed by NiS, and finally the bulk heterojunction of NiS@MoS_2 . These structures are illustrated in [Supplementary Figure 1](#).

To investigate the active sites for the HER, we carefully created surface models of MoS_2 , NiS, and NiS@MoS_2 by cleaving them along the 001, 100, and 001 planes, respectively. The resulting surface models for HER simulations revealed that the side-on heterojunction of $\text{NiS@MoS}_2(001)$ exposes more active sites compared to the top-down heterojunction configuration. After optimization, we established slab models corresponding to $\text{MoS}_2(001)$, $\text{NiS}(100)$, and $\text{NiS@MoS}_2(001)$, as depicted in [Figure 1A](#).

The HER activity of these models was analyzed through Gibbs free energy calculations, using DFT to evaluate the adsorption energies. For this, a single hydrogen atom was placed on the surface of $\text{MoS}_2(001)$, $\text{NiS}(100)$, and $\text{NiS@MoS}_2(001)$ to compute the Gibbs free energy. The computational method applied the Generalized Gradient Approximation (GGA) with the Perdew-Burke-Ernzerhof (PBE) exchange-correlation functional, and a Double-Zeta Polarized (DZP) basis set was used for structure and energy optimization. The Linear Combination of Atomic Orbitals (LCAO) method was applied for Ni, Mo, S, and H atoms. A $5 \times 5 \times 1$ Monkhorst-Pack k-point grid was utilized for structure optimization, while a $5 \times 5 \times 5$ grid was employed for electronic property simulations.

The primary mechanism for the HER on these surfaces was evaluated using a three-state model: H^+ , H^* , and $1/2\text{H}_2$. The Gibbs free energy for hydrogen adsorption (ΔGH^*) is a critical parameter indicating the efficiency of an electrocatalyst. Positive ΔGH^* values suggest slow hydrogen adsorption kinetics, while negative values imply slow hydrogen desorption. Ideal catalysts, such as platinum, have ΔGH^* values close to zero. ΔGH^* is calculated as follows:

$$\Delta\text{G}_{\text{H}^*} = \Delta\text{E}_{\text{H}^*} + \Delta\text{E}_{\text{ZPE}} - T\Delta\text{S}_{\text{H}} \quad (1)$$

where $\Delta\text{E}_{\text{H}^*}$ represents the energy change associated with hydrogen adsorption, $\Delta\text{E}_{\text{ZPE}}$ is the zero-point energy correction, and $\Delta\text{S}_{\text{H}}$ is the entropy change. Room temperature (298.15 K) is used for these calculations, and the NIST database is referenced for entropy data. The relationship between free energy and hydrogen adsorption energy is given by:

$$\Delta\text{E}_{\text{H}^*} = \text{E}_{(\text{H}^*)} - \text{E}_{(\text{H}^+)} - 1/2\text{E}_{\text{H}_2} \quad (2)$$

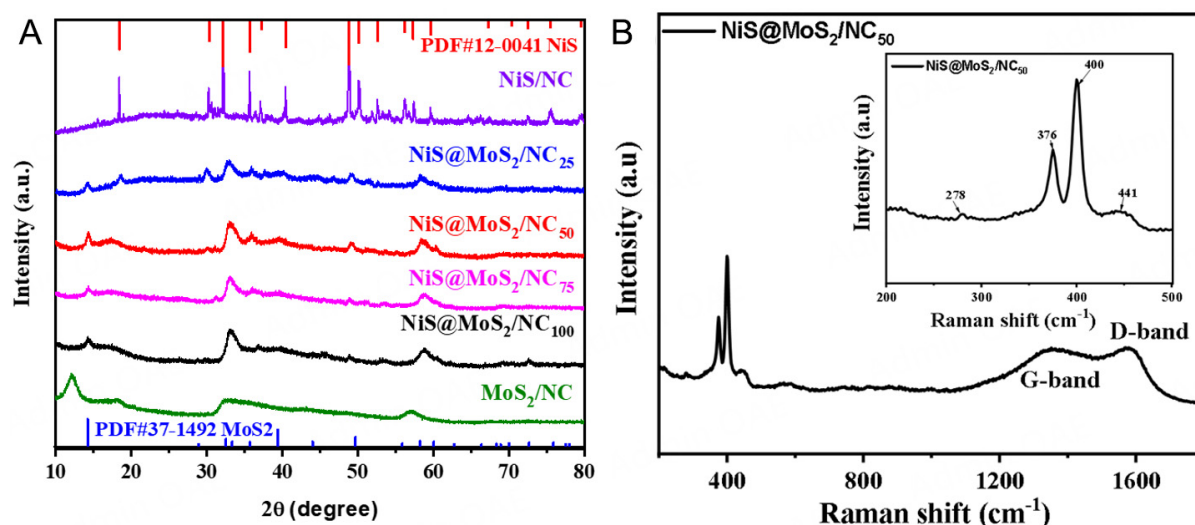


Figure 1. (A) X-ray diffraction (XRD) patterns of the samples and (B) the Raman spectra of NiS@MoS₂/NC₅₀.

where $E_{(H^+)}$ is the energy of the surface with an adsorbed hydrogen atom, $E_{(c)}$ is the energy of the clean surface, and E_{H_2} is the energy of molecular hydrogen. The simplified expression for ΔG_{H^+} is:

$$\Delta G_{H^+} = \Delta E_{H^+} + 0.37 \text{ eV} \quad (3)$$

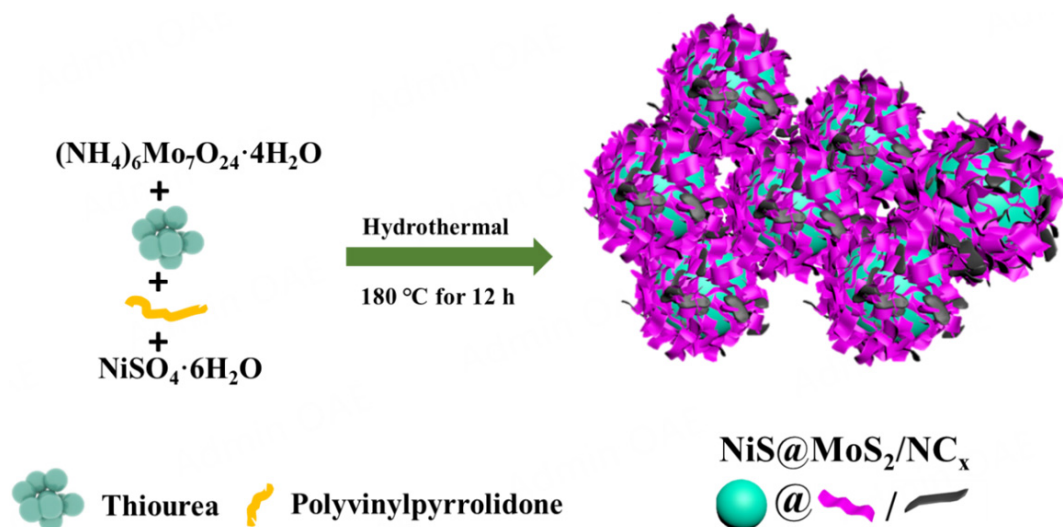
which represents the free energy for hydrogen adsorption and is used to assess the catalyst's effectiveness for HER.

RESULTS AND DISCUSSION

Microstructure and composition

The core-shell NiS@MoS₂/NC_x samples were prepared through an *in-situ* hydrothermal strategy as shown in Scheme 1. The dissolved Ni²⁺ ion is attached to the oxygen group of dispersed PVP chains due to electrostatic attraction. At elevated temperatures and high pressures, thiourea undergoes decomposition into sulfur species. The Ni²⁺ ions combine with the S species to nucleate and grow NiS nanoparticles^[44,45]. At the same time, (NH₄)₆Mo₇O₂₄ reacted with S species to form layer MoS₂ nanosheets around NiS nanoparticles and formed a core-shell structure. The PVP chains act as a template and stabilize nanomaterials during the growth process. The long-chain PVP provides steric repulsion between nanomaterials to keep the core-shell structure^[46]. MoS₂, with its intrinsic layered structure, usually forms nanosheets, leading to the core-shell morphology of NiS nanoparticle@MS₂ nanosheets. During the process, PVP controls the size and morphology of the product. Furthermore, PVP can be decomposed into NC during calcination at 600 °C in inert atmosphere^[47,48]. As a result, NiS@MoS₂/NC_x products are formed. For more details of the synthesis process, see the Section "Experimental".

The crystallinity of the as-prepared composites was characterized using XRD [Figure 1A]. The XRD pattern of as-prepared NiS/NC sample displays peaks at 18.4°, 30.1°, 32.3°, 35.7°, 40.4°, 48.7°, 50.2°, and 52.7° which correspond to crystal planes (110), (101), (300), (021), (211), (131), (410), and (401) of NiS, respectively (PDF#12-0041). When Mo and Ni precursors were used in the reaction mixture, some additional XRD patterns appeared at 14.37°, 33.32°, and 58.33°, which correspond to the crystal planes (002), (101), and (110) of 2H-MoS₂ (PDF#37-1492), respectively. These peaks are more prominent in the sample using high concentration Mo precursor in the reaction mixture [Figure 1A]. This suggests that more MoS₂ nanosheets



Scheme 1. Schematic illustration of the synthetic strategy for the NiS@MoS₂/NC₅₀ microspheres.

formed in the composites using high-concentration Mo precursor. The peak of pure MoS₂ nanosheets shifted from 14.37° to a lower angle of about 12.08° compared to the bulk MoS₂; this indicates expanding the interlayer spacing of as-prepared MoS₂ nanosheets^[49]. The XRD pattern of NC is not discernible in all samples, which may be attributed to the amorphous nature inherent in carbon materials.

The Raman spectrum [Figure 1B] shows the structural characteristics of NiS@MoS₂/NC₅₀. There are two characteristic peaks at 1,360 and 1,582 cm⁻¹, which can be assigned to the G and D-bands of carbon materials, respectively^[50]. The peaks at 400 and 376 cm⁻¹ are related to out-of-plane optical vibrations (A_{1g}¹) and in-plane optical (E_{2g}¹) of MoS₂ nanosheets, respectively. The peaks at 441 and 278 cm⁻¹ can be associated with E_{1g} and A_{1g} active vibration modes of Ni-S and provide unsaturated Mo-S edge sites in the composite^[8,42,51].

SEM images of NiS@MoS₂/NC₅₀ composite are shown in Figure 2A and B. The uniform microsphere materials can be observed, and some are agglomerated [Figure 2A]. The surface of the sphere appeared to be a hierarchical nanosheets-like structure [Figure 2B]. The average size of these spheres is around 101.4 nm after the measurement of more than 70 microspheres and the histogram of size distribution is shown in Supplementary Figure 2. The morphology of other samples NiS@MoS₂/NC₂₅ [Supplementary Figure 3], NiS@MoS₂/NC₇₅ [Supplementary Figure 4], and NiS@MoS₂/NC₁₀₀ [Supplementary Figure 5] is similar to that of the NiS@MoS₂/NC₅₀ composite, with the size of these microspheres also in the sub-micrometer range. However, the size and morphology of the microspheres changed without using PVP in the NiS@MoS₂ sample [Figure 2C and D], resulting in much larger particles compared to the NiS@MoS₂/NC_x composites. This suggests that PVP controlled the size and morphology of the hierarchical microspheres in experimental conditions. Additionally, we observed the nanoparticles embedded in NC materials without hierarchical surfaces when (NH₄)₆Mo₇O₂₄·4H₂O precursor was absent from the reaction mixture [Figure 2E and F].

The TEM images of the sample [Figure 3A-E] showcase its hierarchical structure. As shown in Figure 3A, the sample consists of hierarchical microspheres, with some appearing agglomerated. Each microsphere comprises a dense black core surrounded by a transparent shell, as highlighted in Figure 3B. Figure 3C demonstrates a clear interface between NiS and MoS₂, confirming the successful formation of the

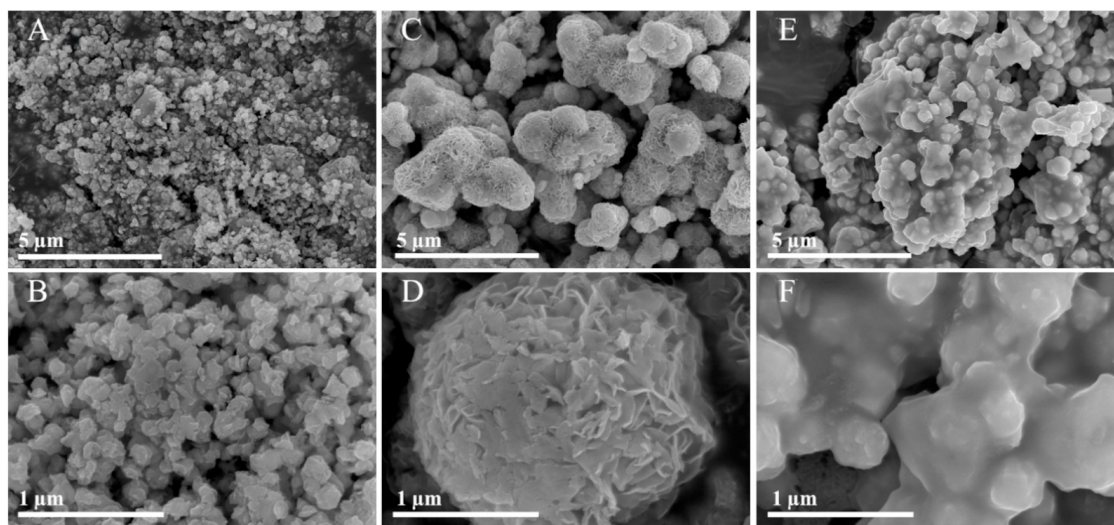


Figure 2. SEM images of (A and B) the NiS@MoS₂/NC₅₀, (C and D) NiS@MoS₂, and (E and F) NiS/NC composites.

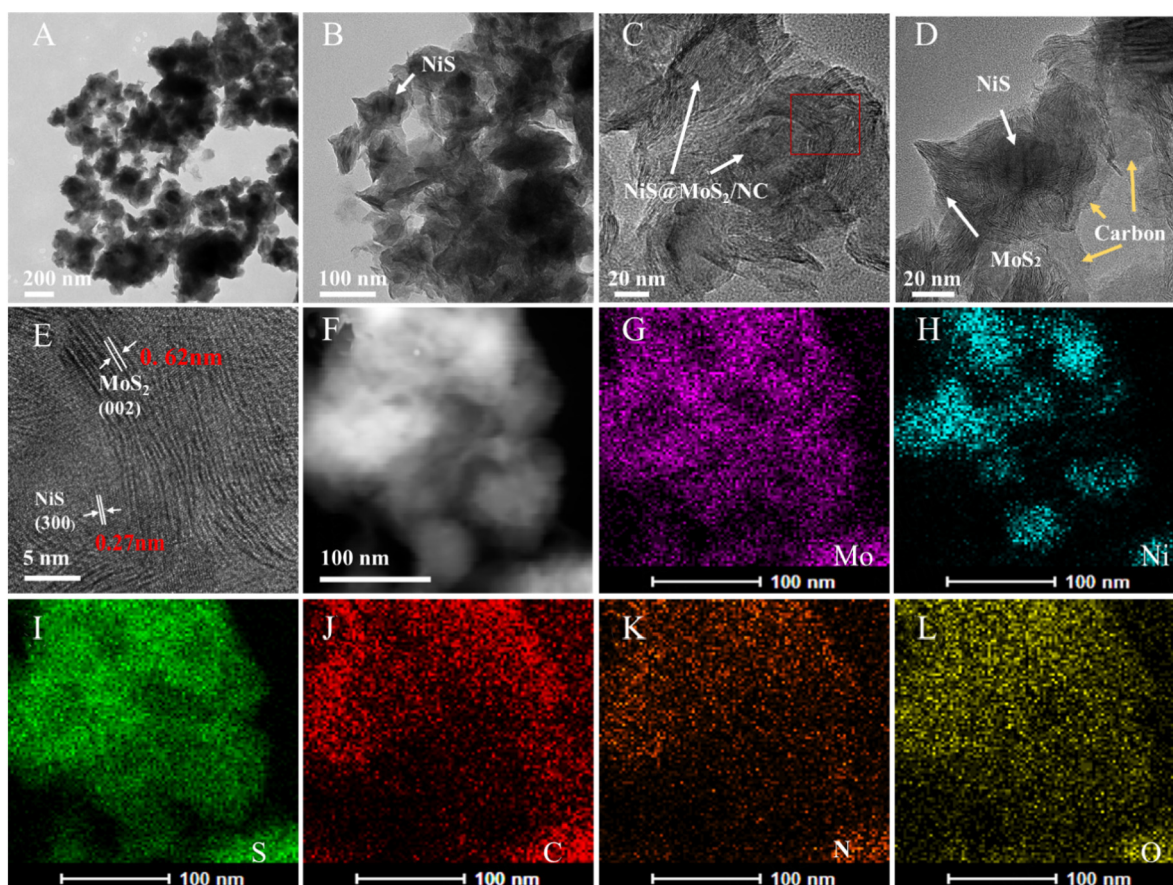


Figure 3. (A and B) TEM and (C-E) HRTEM images of the NiS@MoS₂/NC₅₀ composite. (F) The dark-field TEM image of the NiS@MoS₂/NC₅₀ sample (G-L) and the subsequent EMI of (G) Mo, (H) Ni, (I) S, (J) C, (K) N, (L) O.

heterojunction structure. The shell comprises lamellar nanosheets, while the microsphere's core contains nanoparticles, as indicated by the white arrows in [Figure 3D](#). Furthermore, some non-lamellar materials,

likely NC, are visible in the shell [yellow arrow, Figure 3D], resulting from the conversion of PVP during calcination.

The HRTEM image in Figure 3E provides additional crystallographic insights, revealing an interlayer spacing of 0.62 nm, corresponding to the (002) planes of the MoS₂ nanosheets. The nanoparticle lattice fringes measure approximately 0.27 nm, corresponding to the (300) crystal plane of NiS.

Figure 3F shows the dark-field TEM image, and Figure 3G-L displays elemental mapping images of the NiS@MoS₂/NC₅₀ composite. A stronger Ni signal can be observed in the core of the microsphere, while Mo is mostly distributed in the shell area. The S element signal is stronger in the shell and weaker in the core. The C and N elements are uniformly distributed in the microsphere. These elemental mapping images further revealed the core-shell structure of NiS and MoS₂ in which the NC was distributed. The rise in the O signal may be due to slight oxidation of the composite and/or absorbed water molecules [Figure 3G-L]. The elemental composition determined by energy dispersive X-ray spectrometry (EDS) mapping reveals the following percentages: Mo (10.37%), Ni (6.36%), S (25.66%), C (42.82%), N (2.91%), and O (9.87%). Consequently, the stoichiometric ratio is calculated as 1:0.6:2.5:4.1:0.3:0.9.

For a more precise determination of NC in composite material, the TGA test was measured from 25 to 800 °C under airflow. The weight loss of 6.4% below 400 is possibly due to the evaporation of water molecules from composites^[52]. Further weight loss of about 20.2% from 424 to 500 °C results from the oxidation of carbon materials to CO₂ during the process^[53]. The TGA results suggested that the mass fraction of NC is approximately 20.2 wt% of NiS@MoS₂/NC₅₀ composite [Supplementary Figure 6]. The NC in the spheres may enhance the conductivity of NiS@MoS₂/NC composites.

The surface chemical composition and valence state of elements in NiS@MoS₂/NC_x were analyzed by XPS. The survey XPS spectra of NiS@MoS₂/NC_x composites are shown in Supplementary Figure 7A. Survey XPS spectra of NiS@MoS₂/NC₅₀ composite reveal the presence of Ni, Mo, S, C, N, and O elements. The NiS/NC sample comprises Ni, S, C, N, and O, while the MoS₂/NC catalyst contains Mo, S, C, N, and O elements.

The characteristic peaks of Mo 3d in Figure 4A, derived from the high-resolution spectrum of the NiS@MoS₂/NC₅₀ composite, are observed at 231.1 and 227.97 eV. These peaks correspond to Mo 3d_{3/2} and Mo 3d_{5/2}, respectively, indicating the presence of Mo⁴⁺^[43,54]. The binding energies of Mo 3d_{3/2} and Mo 3d_{5/2} are 230.95 and 227.80 eV, respectively, in the MoS₂/NC sample. The peaks at 235.17 and 234.08 eV in MoS₂/NC and NiS@MoS₂/NC₅₀ are associated with Mo 3d_{3/2} and Mo 3d_{5/2}, indicating the existence of the Mo⁶⁺ oxidation state and suggesting the partial oxidation of the MoS₂ surface^[55]. These peaks are either very small or absent in the NiS@MoS₂/NC₅₀ composite, revealing reduction of Mo⁶⁺ to Mo⁴⁺ oxidation state of the MoS₂ nanosheets in composites. However, the binding energy peaks of Mo⁴⁺ species in NiS@MoS₂/NC₅₀ composite shift to slightly higher energy compared to the MoS₂/NC sample, indicating electron loss from MoS₂.

The presence of a small peak at 225.23 eV represents the existence of S 2s^[56-58]. The high-resolution XPS spectrum of the Ni 2p region of NiS@MoS₂/NC₅₀ composite exhibits a high-energy band Ni 2p_{1/2} at 871.96 and 874.64 eV and a low-energy band Ni 2p_{3/2} at 853.84 and 856.70 eV corresponding to Ni²⁺ and Ni³⁺, respectively^[59,60], while for NiS/NC sample, binding energy peaks are observed at 871.82 and 874.59 eV for Ni 2p_{1/2}, and at 854.01 and 856.75 eV for Ni 2p_{3/2} [Figure 4B]. The peaks around 880.20 and 862.19 eV can be related to the satellite of Ni 2p. The binding energy of the NiS/NC shifted slightly to low energy compared to NiS@MoS₂/NC₅₀. Additionally, the area of Ni²⁺ peaks in the NiS/NC sample is much larger than the

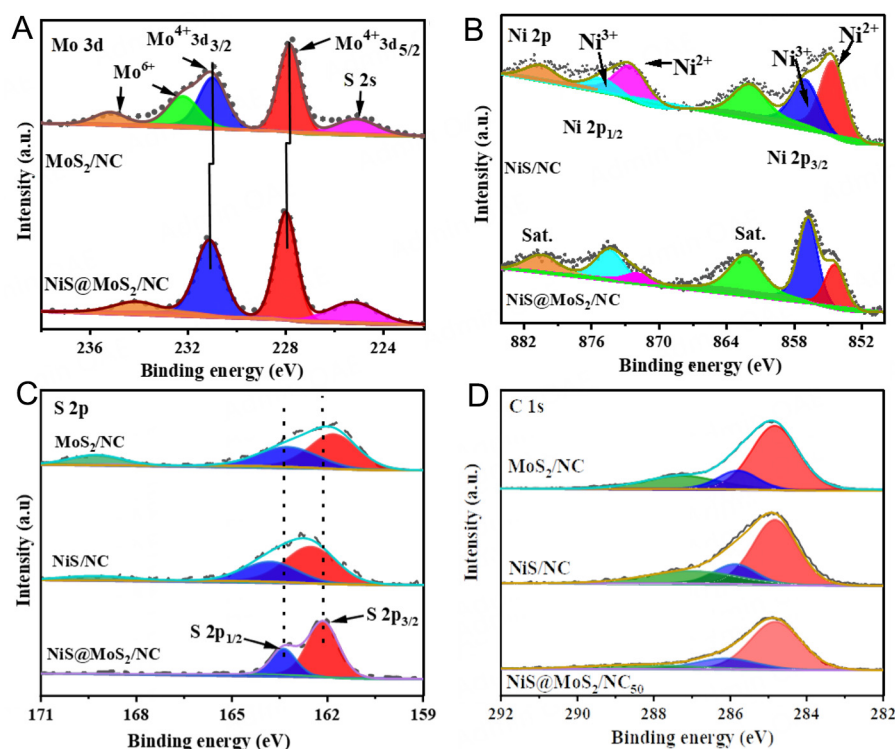


Figure 4. High-resolution XPS spectra of (A) Mo 3d, (B) Ni 2p, (C) S 2p, and (D) C 1s for the NiS@MoS₂/NC₅₀, MoS₂/NC and NiS/NC complexes, respectively.

NiS@MoS₂/NC₅₀ composite, while the opposite is true for Ni³⁺ ions. The XPS spectrum of S 2p can be deconvoluted into spin-orbit doublets, with peaks observed at binding energies of 161.48 and 162.73 eV, corresponding to S 2p_{3/2} and S 2p_{1/2} bands, respectively [Figure 4C]. The binding energies of the S 2p_{3/2} and S 2p_{1/2} bands exhibit a shift towards lower energy in the NiS/C sample, while a shift towards higher energy is observed in the MoS₂/NC catalysts. These results indicate a stronger interaction between MoS₂ and NiS at the heterointerface of NiS@MoS₂/NC₅₀, which may promote the electron transfer from the MoS₂ to the NiS. Furthermore, the changes in density distribution at the heterointerface induce HER performance. Gu *et al.* also observed such phenomena due to the Mott-Schottky effect^[61,62]. The XPS spectrum of C 1s, as illustrated in Figure 4D, reveals a prominent peak at 284.81 eV, indicative of C=C and/or C-C bonds. Additionally, peaks at 286.06 and 288.31 eV, which are of relatively lower intensity, correspond to C-N and C=O bonds, respectively. Notably, these features are scarcely evident in the C 1s spectra across all samples. The N 1s shows the existence of graphitic, pyrrolic, and pyridinic N at a binding energy of 400.8, 399.3, and 398.0 eV, respectively, as presented in Supplementary Figure 7B.

Electrocatalytic performance toward HER

An effective electrocatalyst delivers a low overpotential (η) at a specific current density (J)^[60]. HER performance of the as-prepared NiS@MoS₂/NC_x samples and commercial 20% Pt/C was investigated in 1.0 M KOH solution using a three-electrode setup and loading the same amount of the catalysts on GC electrodes. The polarization curves of the as-prepared samples and commercial Pt/C catalyst are shown in Figure 5A. The commercial 20% Pt/C catalyst exhibits superior HER performance, achieving an overpotential of merely 40 mV at a current density of 10 mA cm⁻². The NiS@MoS₂/NC₅₀ catalyst required an overpotential of only 189 mV at a current density of 10 mA cm⁻² and displays better HER performance than other as-prepared samples [Supplementary Table 2]. NiS@MoS₂/NC₅₀ displays competitive or superior HER

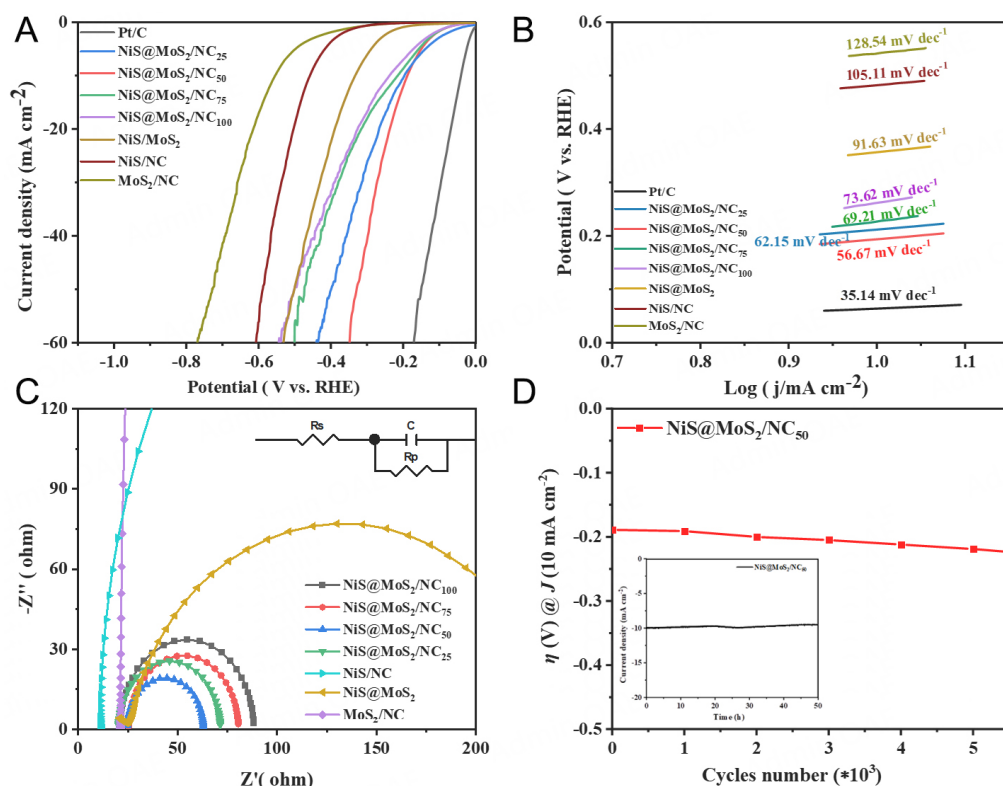


Figure 5. (A) The LSV curves of the commercial Pt/C and NiS@MoS₂/NC_x catalysts, (B) the Tafel plots estimated from LSV graph. (C) The Nyquist plots of the samples and the corresponding circuit in the inset of "C". (D) Potential (V vs. HER) at a 10 mA cm^{-2} current density of the NiS@MoS₂/NC₅₀ catalyst before and after 1,000-5,000 CV cycles and the chronoamperometric curve shown in the inset of "D".

performance 189 $\text{mV}@-10 \text{ mA cm}^{-2}$ than those of reported NiS and MoS₂-based electrocatalysts [Supplementary Table 3]. The NiS@MoS₂/NC₂₅, NiS@MoS₂/NC₇₅, and NiS@MoS₂/NC₁₀₀ composites required an overpotential of 197, 215, and 238 mV at the current density of 10 mA cm^{-2} , respectively. However, NiS/NC (464 mV) and MoS₂/NC (555 mV) alone show poor HER performance at the current density 1 of 0 mV cm^{-2} as the XPS spectra suggest that a strong interaction exists between MoS₂ nanosheets and NiS materials and modulates electronic density distribution at the heterointerface, which may enhance HER performance. The NiS/MoS₂ sample, lacking NC, exhibits an overpotential of 333 mV at a current density of 10 mA cm^{-2} . The superior HER performance of the optimized NiS@MoS₂/NC₅₀ sample can be attributed to the synergistic interactions at the heterointerfaces between MoS₂ nanosheets and NiS nanoparticles, the improved conductivity imparted by the NC within the composite, and the optimized ratio of MoS₂ to NiS components.

The Tafel plots are derived from LSV curves to study the reaction kinetics and mechanism of the catalysts. The Pt/C exhibits the smallest Tafel slope of 35.14 mV dec^{-1} . Among the as-prepared samples, the Tafel slope of the NiS@MoS₂/NC₅₀ sample is 56.67 mV dec^{-1} , smaller than those of NiS@MoS₂/NC₁₀₀, NiS@MoS₂/NC₇₅, NiS@MoS₂/NC₂₅, NiS/MoS₂, NiS/NC, MoS₂/NC electrocatalysts while being close to that of Pt/C [Figure 5B] in 1.0 M KOH solution. A small Tafel slope is conducive to practical application since it will lead to a faster increment of HER rate with low overpotential.

The electrochemical surface area (ECSA) of various samples was determined by measuring the electrochemical C_{dl} . This was achieved by conducting CV within a non-Faradaic region at varying scan rates ranging from 10 to 100 mV/s, as illustrated in [Supplementary Figure 8A-G](#). All the NiS@MoS₂/NC_x composites samples exhibited higher C_{dl} values than NiS/NC and MoS₂/NC, indicating the presence of more active sites for electrochemical catalytic activity, possibly due to heterointerfaces. The NiS@MoS₂/NC₅₀ samples showed the highest C_{dl} electrochemical active sites for enhanced HER performance and indicated the amount of heterointerfaces in the sample [[Supplementary Figure 8H](#)]. The C_{dl} values for the samples NiS@MoS₂/NC₁₀₀, NiS@MoS₂/NC₇₅, NiS@MoS₂/NC₅₀, NiS@MoS₂/NC₂₅, NiS/NC, MoS₂/NC, and NiS@MoS₂ are 3.49, 3.97, 8.18, 5.22, 2.18, 1.98, and 2.65 mF cm⁻², respectively. Notably, NiS@MoS₂/NC₅₀ exhibits a higher number of catalytic active sites compared to the other NiS@MoS₂/NC_x, NiS/NC, and MoS₂/NC composites, suggesting enhanced electrochemical catalytic activity, likely due to the presence of heterointerfaces. The ECSA-normalized LSV curves were calculated to demonstrate the intrinsic activity of catalysts [[Supplementary Figure 9](#)]. The results show that the NiS@MoS₂/NC₅₀ sample exhibits the highest intrinsic activity. However, electrochemical performance is influenced, especially at high current density, by other factors beyond intrinsic activity, such as mass transport limitations, catalyst morphology, and the specific distribution of active sites.

The EIS [[Figure 5C](#)] tests were conducted to assess the catalytic activity at the electrode/electrolyte interface. The samples showed potential in the HER catalysis when the EIS revealed low charge-transfer resistance. The Nyquist plots are analyzed using the equivalent circuit depicted in [Figure 5C](#). The charge transfer resistance (R_{ct}) of NiS@MoS₂/NC₁₀₀, NiS@MoS₂/NC₇₅, NiS@MoS₂/NC₅₀, NiS@MoS₂/NC₂₅, NiS@MoS₂, NiS/NC and MoS₂/NC composites is 67.23, 55.29, 38.88, 51.15, 204.3, 586.3, and 737.2 Ω, respectively. NiS@MoS₂/NC₅₀ exhibited a lower R_{ct} value than other samples, indicating more efficient charge transfer at the electrode/electrolyte interface for improved catalytic performance^[63].

Another crucial factor for evaluating the performance of an electrocatalyst is stability [[Figure 5D](#)]. NiS@MoS₂/NC₅₀ was used to observe its stability by CV. The LSV curves of NiS@MoS₂/NC₅₀ catalysts before and after various cycles are shown in [Supplementary Figure 10](#). The material required a slightly high overpotential at a current density of 10 mV cm⁻² after 1,000, 2,000, 3,000, 4,000, and 5,000 CV cycles.

[Supplementary Figure 10A](#) shows almost negligible degradation of the composite after CV cycles. The continuous CV scanning and chronoamperometry response were also executed to further assess the durability of the as-prepared NiS@MoS₂/NC₅₀. As shown in [Supplementary Figure 10B](#), after the stability test, the NiS@MoS₂/NC₅₀ electrode almost retains the initial activity, suggesting splendid electrochemical durability. XRD patterns of NiS@MoS₂/NC₅₀ composites before and after 5,000 CV are shown in [Supplementary Figure 11](#). The main peaks of MoS₂ and NiS phases can be seen in the XRD pattern, and no obvious changes are observed [[Supplementary Figure 11](#)]. The SEM images confirmed the microsphere morphology of NiS@MoS₂/NC₅₀ before and after 5,000 CV cycles [[Supplementary Figure 12](#)]. However, the nanosheets are not as clear and obvious compared to the fresh NiS@MoS₂/NC₅₀ sample. Furthermore, TEM images of the sample display a hierarchical microsphere-like structure, and some of them are agglomerated. It can be seen as a dense black center and transparent periphery [[Supplementary Figure 13](#)]. These results indicate that the sample is a highly stable catalyst for electrochemical HER performance in an alkaline environment. Moreover, the amperometry test was measured to further assess the durability of the NiS@MoS₂/NC₅₀. The amperometry curve (inset of [Figure 5D](#)) indicates that the current density of NiS@MoS₂/NC₅₀ exhibits a negligible decay after continuous electrolysis for 50 h at an applied potential, further revealing the superior HER stability. The LSV curves of NiS@MoS₂/NC₅₀ before and after the amperometry test almost show the same HER catalytic activity.

First-principle density functional theory simulations

First-principles DFT simulations were used to investigate the HER performance of NiS@MoS₂, NiS, and MoS₂. These simulations examined the free energy of hydrogen adsorption (ΔG_{H^+}) of Mo, Ni, and S elements active sites in different NiS@MoS₂, NiS, and MoS₂ catalysts and identified the highest active site in these materials (Figure 6A and calculation details in the Section "Computational approach"). The results revealed that NiS@MoS₂ has significantly better HER performance compared to NiS and MoS₂ due to optimal charge transfer within the heterojunction. Specifically, the ΔG_{H^+} values on sulfur sites for MoS₂ and NiS are -1.760 and -1.95 eV, respectively. However, in NiS@MoS₂, the ΔG_{H^+} values on sulfur are -0.19 and 0.52 eV bonded with Mo and Ni sites, indicating that this structure has a more favorable energy profile for HER.

Additionally, the ΔG_{H^+} values for hydrogen evolution at metal sites in MoS₂, NiS, and NiS@MoS₂ were 1.12, -2.94, 0.04, and -0.29 eV, respectively. The optimal ΔG_{H^+} value for an electrocatalyst should be moderate, providing a balance between hydrogen adsorption and desorption. The results suggest that the ΔG_{H^+} value at the Mo site in NiS@MoS₂ is near the ideal thermodynamic limit, reinforcing its potential as a superior catalyst for HER.

The Electron localization function (ELF) maps [Figure 6B] indicate that the NiS@MoS₂ surface is more electron-rich compared to pristine MoS₂ and NiS, suggesting electron interaction between Ni and Mo in the NiS@MoS₂ composites [Supplementary Figure 14]. The electron difference density (EDD) analysis shows that the NiS@MoS₂ composite has an optimal electron distribution, supporting its catalytic efficiency. Pristine MoS₂ has low EDD, leading to weaker hydrogen adsorption, while NiS, with high EDD, has strong hydrogen adsorption ($\Delta G_{H^+} = -2.94$ eV).

Furthermore, Density of states (DOS) plots in Figure 7A-C show that the valence and conduction bands in MoS₂ are separated by a bandgap, while it has a narrower bandgap. In NiS@MoS₂ composites, strong hybridization of bonding and antibonding orbitals results in the disappearance of the bandgap, promoting efficient charge transfer and increased stability. This charge transfer leads to a decrease in work function from 6.41 eV in MoS₂ to 4.81 eV in NiS@MoS₂, as shown in the effective potential plot [Figure 7D]. The local dipole generated by this charge transfer, especially at the Mo site, enhances chemical reactivity in the interface region of NiS@MoS₂ composite, resulting in an ideal ΔG_{H^+} value of 0.04 eV. Overall, the DFT simulations confirm that enhanced HER activity of NiS@MoS₂ composite can be attributed to the strong interaction between NiS nanoparticles and MoS₂ nanosheets and charge transfer characteristics of NiS@MoS₂ contribute to its outstanding performance as an electrocatalyst for HER. The NC in the spheres may enhance the conductivity of NiS@MoS₂/NC composites.

CONCLUSION

In conclusion, a NiS@MoS₂/NC core-shell microsphere was effectively synthesized as a high-performance electrocatalyst for HER through the hydrothermal method. The morphology and size of the NiS@MoS₂/NC catalyst were controlled by PVP in the composite materials. Among the prepared samples, the NiS@MoS₂/NC₅₀ composite exhibits excellent HER performance with an overpotential of 189 mV at a current density of 10 mA cm⁻², a small Tafel slope of 56.67 mV dec⁻¹, and good stability of HER in 1.0 M KOH solution. DFT simulations corroborate the exceptional catalytic performance of NiS@MoS₂, attributed to the optimal charge transfer between NiS nanoparticles and MoS₂ nanosheets. This electron transfer mechanism promotes effective H⁺ interaction and adsorption at the Mo site of NiS@MoS₂, resulting in a reduced Gibbs free energy ($\Delta G_{H^+}^* \approx 0.04$ eV) and local work function at the heterointerface, thereby enhancing the HER performance. This study provides an *in-situ* strategy to design and prepare other core-shell metal sulfide electrocatalysts for enhanced HER performance and stability.

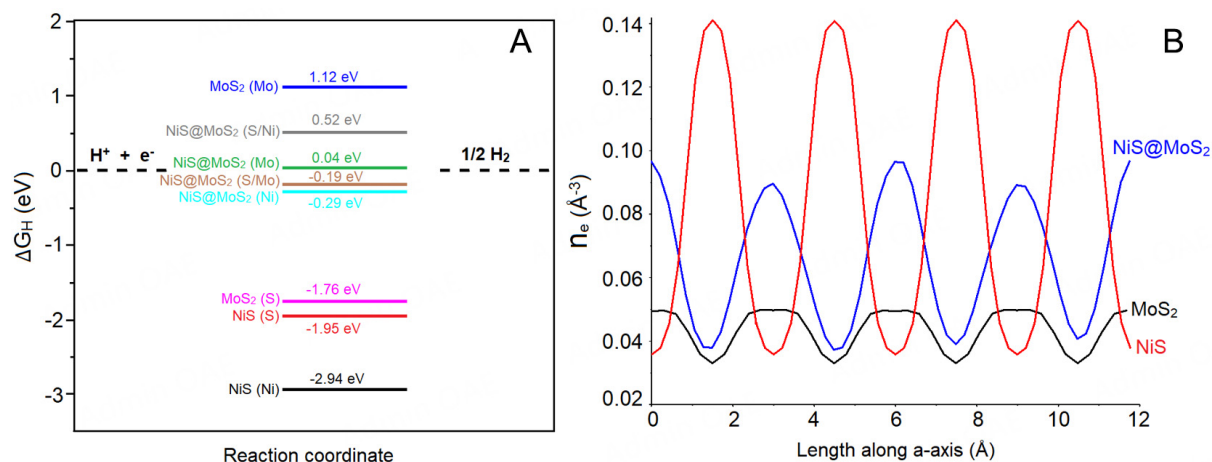


Figure 6. (A) Gibbs free energy diagram of hydrogen adsorption on active sites of MoS₂, NiS, and NiS@MoS₂ (B), and EDD of MoS₂, NiS, and NiS@MoS₂ samples.

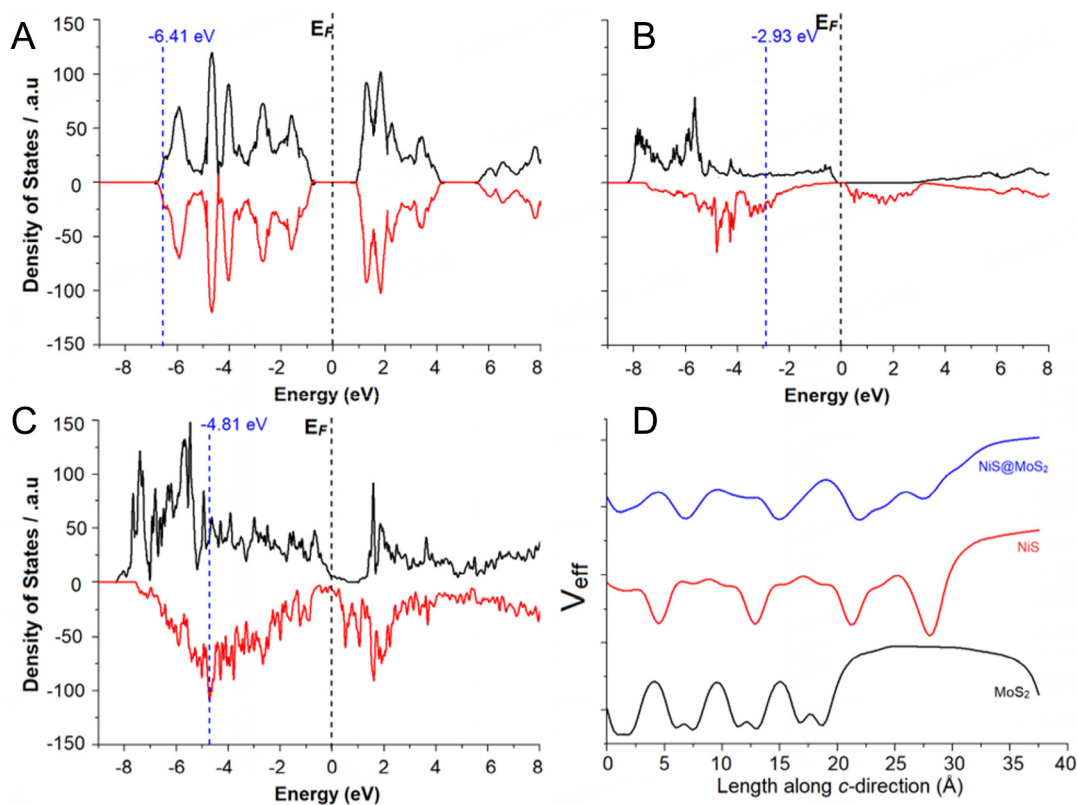


Figure 7. The density of States plots of MoS₂ (A), NiS (B), and NiS@MoS₂ (C), the values in these plots are Fermi Energy and where the Fermi level is set to zero. (D) Comparative 2D effective potential plots of MoS₂, NiS, and NiS@MoS₂.

DECLARATIONS

Acknowledgments

We would like to thank the National Natural Science Foundation of China (under research grant no. 22150410332) and the start-up foundation for the introduction of talent at Jiangsu University of Science and Technology, China. We also acknowledge the Faculty of Environment, Science and Economy, University of

Exeter, UK, and funding support from the Engineering and Physical Sciences Research Council (EPSRC). Additionally, we appreciate the use of the University of Exeter's Advanced Research Computing facilities (Athena HPC Cluster) for this work and for the provision of QuantumATK_2019.12 software. For the purpose of open access, the authors have applied a Creative Commons Attribution (CC BY) license to any Author Accepted Manuscript version arising from this work.

Authors' contributions

Data curation, writing - original draft: Obiang Nsang, G. E.

Data curation, visualization: Ullah, B.

Visualization, investigation: Hua, S.; Dike, F. N.

Supervision, conceptualization, revised draft, methodology: Shah, S. A.

Methodology: Khan, N.

Visualization: Ullah, N. (Nabi Ullah); Ullah, N. (Noor Ullah)

Visualization, review draft: Yaseen, W.

Supervision, review & editing: Yuan, A.

DFT simulations, supervision, review & editing, validation: Ullah, H.

Availability of data and materials

The data is available upon request from the authors.

Financial support and sponsorship

The funding from the the National Natural Science Foundation of China (under research grant no. 22150410332) and the start-up foundation for the introduction of talent at Jiangsu University of Science and Technology, China, The Faculty of Environment, Science and Economy, University of Exeter, UK and funding support from the Engineering and Physical Sciences Research Council (EPSRC).

Conflicts of interest

All authors declared that there are no conflicts of interest.

Ethical approval and consent to participate

Not applicable.

Consent for publication

Not applicable.

Copyright

© The Author(s) 2025.

REFERENCES

1. Morales-Guio, C. G.; Stern, L. A.; Hu, X. Nanostructured hydrotreating catalysts for electrochemical hydrogen evolution. *Chem. Soc. Rev.* **2014**, *43*, 6555-69. DOI PubMed
2. Āurovič, M.; Hnát, J.; Bouzek, K. Electrocatalysts for the hydrogen evolution reaction in alkaline and neutral media. A comparative review. *J. Power. Sources.* **2021**, *493*, 229708. DOI
3. Shang, X.; Tang, J.; Dong, B.; Sun, Y. Recent advances of nonprecious and bifunctional electrocatalysts for overall water splitting. *Sustain. Energy. Fuels.* **2020**, *4*, 3211-28. DOI
4. Li, X.; Zhao, L.; Yu, J.; et al. Water splitting: from electrode to green energy system. *Nanomicro. Lett.* **2020**, *12*, 131. DOI PubMed PMC
5. Ahmed, I.; Biswas, R.; Iqbal, M.; Roy, A.; Haldar, K. K. NiS/MoS₂ anchored multiwall carbon nanotube electrocatalyst for hydrogen generation and energy storage applications. *ChemNanoMat* **2023**, *9*, e202200550. DOI
6. Mistry, K.; Jalja; Lakhani, R.; Tripathi, B.; Shinde, S.; Chandra, P. Recent trends in MXene/Metal chalcogenides for electro-/

- photocatalytic hydrogen evolution reactions. *Int. J. Hydrogen. Energy.* **2022**, 47, 41711-32. DOI
7. Shah, S. A.; Shen, X.; Xie, M.; et al. Nickel@Nitrogen-doped carbon@MoS₂ nanosheets: an efficient electrocatalyst for hydrogen evolution reaction. *Small* **2019**, 15, e1804545. DOI
 8. Liu, G.; Thummavichai, K.; Lv, X.; et al. Defect-rich heterogeneous MoS₂/rGO/NiS nanocomposite for efficient pH-universal hydrogen evolution. *Nanomaterials* **2021**, 11, 662. DOI PubMed PMC
 9. Lin, J.; Wang, P.; Wang, H.; et al. Defect-rich heterogeneous MoS₂/NiS₂ nanosheets electrocatalysts for efficient overall water splitting. *Adv. Sci.* **2019**, 6, 1900246. DOI PubMed PMC
 10. Zhang, J.; Wang, Y.; Cui, J.; et al. In-situ synthesis of carbon-coated β -NiS nanocrystals for hydrogen evolution reaction in both acidic and alkaline solution. *Int. J. Hydrogen. Energy.* **2018**, 43, 16061-7. DOI
 11. Zheng, J.; Sheng, W.; Zhuang, Z.; Xu, B.; Yan, Y. Universal dependence of hydrogen oxidation and evolution reaction activity of platinum-group metals on pH and hydrogen binding energy. *Sci. Adv.* **2016**, 2, e1501602. DOI PubMed PMC
 12. Strmcnik, D.; Lopes, P. P.; Genorio, B.; Stamenkovic, V. R.; Markovic, N. M. Design principles for hydrogen evolution reaction catalyst materials. *Nano. Energy.* **2016**, 29, 29-36. DOI
 13. Han, N.; Zhang, X.; Zhang, C.; et al. Lowering the kinetic barrier via enhancing electrophilicity of surface oxygen to boost acidic oxygen evolution reaction. *Matter* **2024**, 7, 1330-43. DOI
 14. Hua, W.; Sun, H.; Xu, F.; Wang, J. A review and perspective on molybdenum-based electrocatalysts for hydrogen evolution reaction. *Rare. Met.* **2020**, 39, 335-51. DOI
 15. Qin, Q.; Chen, L.; Wei, T.; Liu, X. MoS₂/NiS yolk-shell microsphere-based electrodes for overall water splitting and asymmetric supercapacitor. *Small* **2019**, 15, e1803639. DOI
 16. Koh EW, Chiu CH, Lim YK, Zhang Y, Pan H. Hydrogen adsorption on and diffusion through MoS₂ monolayer: first-principles study. *Int. J. Hydrogen. Energy.* **2012**, 37, 14323-8. DOI
 17. Liu, Q.; Fang, Q.; Chu, W.; et al. Electron-doped 1T-MoS₂ via interface engineering for enhanced electrocatalytic hydrogen evolution. *Chem. Mater.* **2017**, 29, 4738-44. DOI
 18. Xie, J.; Zhang, J.; Li, S.; et al. Controllable disorder engineering in oxygen-incorporated MoS₂ ultrathin nanosheets for efficient hydrogen evolution. *J. Am. Chem. Soc.* **2013**, 135, 17881-8. DOI
 19. Kim, Y.; Jackson, D. H. K.; Lee, D.; et al. In situ electrochemical activation of atomic layer deposition coated MoS₂ basal planes for efficient hydrogen evolution reaction. *Adv. Funct. Mater.* **2017**, 27, 1701825. DOI
 20. Geng, S.; Liu, Y.; Yu, Y. S.; Yang, W.; Li, H. Engineering defects and adjusting electronic structure on S doped MoO₂ nanosheets toward highly active hydrogen evolution reaction. *Nano. Res.* **2020**, 13, 121-6. DOI
 21. Meng, X.; Yu, L.; Ma, C.; et al. Three-dimensionally hierarchical MoS₂/graphene architecture for high-performance hydrogen evolution reaction. *Nano. Energy.* **2019**, 61, 611-6. DOI
 22. Sun, Y.; Alimohammadi, F.; Zhang, D.; Guo, G. Enabling colloidal synthesis of edge-oriented MoS₂ with expanded interlayer spacing for enhanced HER catalysis. *Nano. Lett.* **2017**, 17, 1963-9. DOI
 23. Li, W.; Zhang, Z.; Zhang, W.; Zou, S. MoS₂ nanosheets supported on hollow carbon spheres as efficient catalysts for electrochemical hydrogen evolution reaction. *ACS. Omega.* **2017**, 2, 5087-94. DOI PubMed PMC
 24. Zhang, X.; Hua, S.; Lai, L.; et al. Strategies to improve electrocatalytic performance of MoS₂-based catalysts for hydrogen evolution reactions. *RSC. Adv.* **2022**, 12, 17959-83. DOI PubMed PMC
 25. Li, Z.; Xu, Y.; Ren, X.; Wang, W. Facile synthesis of NiS₂-MoS₂ heterostructured nanoflowers for enhanced overall water splitting performance. *J. Mater. Sci.* **2020**, 55, 13892-904. DOI
 26. Xu, X.; Zhong, W.; Zhang, X.; et al. Flexible symmetric supercapacitor with ultrahigh energy density based on NiS/MoS₂@N-rGO hybrids electrode. *J. Colloid. Interface. Sci.* **2019**, 543, 147-55. DOI
 27. Zhang, D.; Jin, Y.; Cao, Y. Facile synthesis and ammonia gas sensing properties of NiO nanoparticles decorated MoS₂ nanosheets heterostructure. *J. Mater. Sci. Mater. Electron.* **2019**, 30, 573-81. DOI
 28. Zhao, X.; Ran, W.; Wang, Z.; Sun, J.; Liu, R.; Liu, J. Dynamic monitoring of the structural evolution of Au@Pd under electrochemistry. *J. Phys. Chem. C.* **2023**, 127, 5432-41. DOI
 29. Jiao, J.; Yang, W.; Pan, Y.; et al. Interface engineering of partially phosphidated Co@Co-P@NPCNTs for highly enhanced electrochemical overall water splitting. *Small* **2020**, 16, e2002124. DOI
 30. Zhang, B.; Shan, J.; Wang, W.; Tsiakaras, P.; Li, Y. Oxygen vacancy and core-shell heterojunction engineering of anemone-like CoP@CoOOH bifunctional electrocatalyst for efficient overall water splitting. *Small* **2022**, 18, e2106012. DOI
 31. Gao, Y.; Zhang, D.; Li, J.; et al. The core/shell structure P doped MoS₂@Ni₃S₂ nanorods array for high current density hydrogen evolution in alkaline and acidic electrolyte. *Chemistry* **2022**, 28, e202202410. DOI
 32. Kobayashi, Y.; Yokoyama, S.; Shoji, R. Molten salt synthesis of intermetallic compound TiNi nanopowder passivated by TiO_x shell prepared from NiTiO₃ for catalytic hydrogenation. *Materials* **2022**, 15, 8536. DOI PubMed PMC
 33. Wang, H.; Jiao, S.; Liu, S.; et al. Mesoporous bimetallic Au@Rh core-shell nanowires as efficient electrocatalysts for pH-universal hydrogen evolution. *ACS. Appl. Mater. Interfaces.* **2021**, 13, 30479-85. DOI
 34. Wang, H.; Tian, L.; Zhao, X.; Ali, M.; Yin, K.; Xing, Z. In situ growth MoS₂/NiS composites on Ni foam as electrode materials for supercapacitors. *Mater. Today. Commun.* **2023**, 34, 105041. DOI
 35. Tang, C.; Zhang, H.; Xu, K.; et al. Scalable synthesis of heterostructure molybdenum and nickel sulfides nanosheets for efficient hydrogen generation in alkaline electrolyte. *Catal. Today.* **2018**, 316, 171-6. DOI

36. Yin, M.; Zhang, W.; Qiao, F.; Sun, J.; Fan, Y.; Li, Z. Hydrothermal synthesis of MoS₂-NiS/CdS with enhanced photocatalytic hydrogen production activity and stability. *J. Solid. State. Chem.* **2019**, *270*, 531-8. DOI
37. Chen, Z.; Liu, X.; Xin, P.; et al. Interface engineering of NiS@MoS₂ core-shell microspheres as an efficient catalyst for hydrogen evolution reaction in both acidic and alkaline medium. *J. Alloys. Compd.* **2021**, *853*, 157352. DOI
38. Zhao, X.; Bao, J.; Zhou, Y.; et al. Heterostructural MoS₂/NiS nanoflowers via precise interface modification for enhancing electrocatalytic hydrogen evolution. *New. J. Chem.* **2022**, *46*, 5505-14. DOI
39. Patil, P. A.; Khalate, S. A.; Patil, U. M.; Kale, R. D.; Kulkarni, S. B. Cavity structured S-NiO with improved energy density for aqueous asymmetric hybrid supercapacitors by CDA mechanism. *Mater. Adv.* **2023**, *4*, 4607-19. DOI
40. Guan, S.; Fu, X.; Lao, Z.; Jin, C.; Peng, Z. NiS-MoS₂ hetero-nanosheet arrays on carbon cloth for high-performance flexible hybrid energy storage devices. *ACS. Sustain. Chem. Eng.* **2019**, *7*, 11672-81. DOI
41. Tao, K.; Gong, Y.; Lin, J. Low-temperature synthesis of NiS/MoS₂/C nanowires/nanoflakes as electrocatalyst for hydrogen evolution reaction in alkaline medium via calcining/sulfurizing metal-organic frameworks. *Electrochim. Acta.* **2018**, *274*, 74-83. DOI
42. Liu, Y.; Li, Q.; Zhu, Y.; et al. One-step synthesis of MoS₂/NiS heterostructures with a stable 1T phase for an efficient hydrogen evolution reaction. *Dalton. Trans.* **2023**, *52*, 8530-5. DOI
43. Ali, S. S.; Sayyar, R.; Xu, L.; et al. In-situ synthesis of NiS₂ nanoparticles/MoS₂ nanosheets hierarchical sphere anchored on reduced graphene oxide for enhanced electrocatalytic hydrogen evolution reaction. *J. Colloid. Interface. Sci.* **2022**, *624*, 150-9. DOI
44. Lunk, H.; Hartl, H. Discovery, properties and applications of molybdenum and its compounds. *ChemTexts* **2017**, *3*, 48. DOI
45. Luo, W.; Zhang, G.; Cui, Y.; et al. One-step extended strategy for the ionic liquid-assisted synthesis of Ni₃S₄-MoS₂ heterojunction electrodes for supercapacitors. *J. Mater. Chem. A.* **2017**, *5*, 11278-85. DOI
46. Jian, G.; Zhang, C.; Yan, C.; Moon, K.; Wong, C. P. Scalable preparation of fully coated Ag@BaTiO₃ core@shell particles via poly(vinylpyrrolidone) assistance for high-*k* applications. *ACS. Appl. Nano. Mater.* **2018**, *1*, 1396-405. DOI
47. Loria-Bastarrachea, M. I.; Herrera-Kao, W.; Cauich-Rodriguez, J. V.; Cervantes-Uc, J. M.; Vázquez-Torres, H.; Ávila-Ortega, A. A TG/FTIR study on the thermal degradation of poly(vinyl pyrrolidone). *J. Therm. Anal. Calorim.* **2011**, *104*, 737-42. DOI
48. Brzezińska, M.; Szubiakiewicz, E.; Jędrzejczyk, M. Thermal stability of poly(N-vinylpyrrolidone) immobilized on the surface of silica in the presence of noble metals in an atmosphere of hydrogen and oxygen. *Mater. Today. Commun.* **2021**, *26*, 101706. DOI
49. Tang, Y.; Wang, Y.; Wang, X.; et al. Molybdenum disulfide/nitrogen-doped reduced graphene oxide nanocomposite with enlarged interlayer spacing for electrocatalytic hydrogen evolution. *Adv. Energy. Mater.* **2016**, *6*, 1600116. DOI
50. Indhumathy, M.; Prakasam, A. Controllable synthesis of NiS/rGO hybrid composite: an excellent counter electrode for dye sensitized solar cell. *J. Clust. Sci.* **2020**, *31*, 91-8. DOI
51. Abhiram, N.; Thangaraju, D.; Marnadu, R.; et al. Structural, vibrational, morphological, optical and electrical properties of NiS and fabrication of SnS/NiS nanocomposite for photodetector applications. *Inorg. Chem. Commun.* **2021**, *133*, 108882. DOI
52. Xu, C.; Wang, X.; Zhu, J.; Yang, X.; Lu, L. Deposition of Co₃O₄ nanoparticles onto exfoliated graphite oxide sheets. *J. Mater. Chem.* **2008**, *18*, 5625. DOI
53. Wang, G.; Yang, J.; Park, J.; et al. Facile synthesis and characterization of graphene nanosheets. *J. Phys. Chem. C.* **2008**, *112*, 8192-5. DOI
54. Zhai, Z.; Li, C.; Zhang, L.; et al. Dimensional construction and morphological tuning of heterogeneous MoS₂/NiS electrocatalysts for efficient overall water splitting. *J. Mater. Chem. A.* **2018**, *6*, 9833-8. DOI
55. Ali, S. S.; Xu, L.; Sayyar, R.; et al. Growth of MoS₂ nanosheets on M@N-doped carbon particles (M = Co, Fe or CoFe alloy) as an efficient electrocatalyst toward hydrogen evolution reaction. *Chem. Eng. J.* **2022**, *428*, 132126. DOI
56. Yang, Y.; Zhang, K.; Lin, H.; et al. MoS₂-Ni₃S₂ heteronanorods as efficient and stable bifunctional electrocatalysts for overall water splitting. *ACS. Catal.* **2017**, *7*, 2357-66. DOI
57. Gong, Y.; Yang, Z.; Lin, Y.; et al. Correction: Controlled synthesis of bifunctional particle-like Mo/Mn-Ni_xS_y/NF electrocatalyst for highly efficient overall water splitting. *Dalton. Trans.* **2019**, *48*, 7025. DOI
58. Wei, H.; Tan, A.; Liu, W.; et al. Interface engineering-induced 1T-MoS₂/NiS heterostructure for efficient hydrogen evolution reaction. *Catalysts* **2022**, *12*, 947. DOI
59. Voiry, D.; Yamaguchi, H.; Li, J.; et al. Enhanced catalytic activity in strained chemically exfoliated WS₂ nanosheets for hydrogen evolution. *Nat. Mater.* **2013**, *12*, 850-5. DOI
60. Huang, H.; Zhao, Y.; Bai, Y.; Li, F.; Zhang, Y.; Chen, Y. Conductive metal-organic frameworks with extra metallic sites as an efficient electrocatalyst for the hydrogen evolution reaction. *Adv. Sci.* **2020**, *7*, 2000012. DOI PubMed PMC
61. Huang, L.; Li, Z.; Sun, S.; et al. NiS/MoS₂ complex grown on carbon paper as a bifunctional electrocatalyst for full water splitting. *J. Alloys. Compd.* **2022**, *926*, 166870. DOI
62. Gu, C.; Zhou, G.; Yang, J.; et al. NiS/MoS₂ mott-schottky heterojunction-induced local charge redistribution for high-efficiency urea-assisted energy-saving hydrogen production. *Chem. Eng. J.* **2022**, *443*, 136321. DOI
63. Bao, F.; Kemppainen, E.; Dorbandt, I.; et al. Understanding the hydrogen evolution reaction kinetics of electrodeposited nickel-molybdenum in acidic, near-neutral, and alkaline conditions. *ChemElectroChem* **2021**, *8*, 195-208. DOI